CHEMISTRY OF MATERIALS

Article

pubs.acs.org/cm

Graphene Oxide Assisted Synthesis of Self-assembled Zinc Oxide for Lithium-Ion Battery Anode

Chungho Kim, Jin Wook Kim, Hyunhong Kim, Dong Hyeon Kim, Changhoon Choi, Yoon Seok Jung, and Jongnam Park*

School of Energy and Chemical Engineering, Ulsan National Institute of Science and Technology (UNIST), Ulsan 689-798, Republic of Korea

Supporting Information

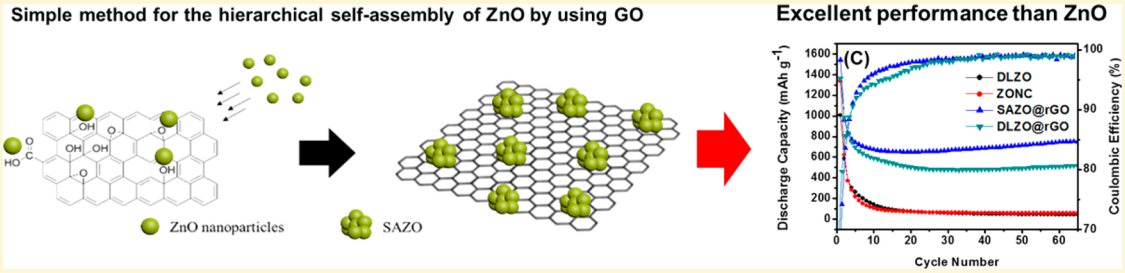

ABSTRACT: A simple method for the synthesis of a hierarchically self-assembled zinc oxide is presented, in which graphene oxide is used to assist in the assembly of the structure and improve the electrical conductivity of the ZnO. The self-assembled ZnO formed on graphene oxide exhibits a high specific capacity, while also demonstrating good rate performance and cycling stability due to the advantages of using both nanoparticles and a secondary structure.

1. INTRODUCTION

Nanostructured materials have been receiving increasing attention in recent years because of the interesting mechanical, optical, and electrical properties that such materials offer.[1−3] In particular, the development of nanostructured electrodes for lithium-ion batteries has attracted the interest of a number of researchers due to the advantages offered in terms of new reaction mechanisms that are not possible with bulk materials, better buffering of volume expansion, and shorter pathways for Li^+ ion and electron transport.[2,4−8] However, the commercial application of such materials requires overcoming the challenges such as poor cycle retention due to an increase in undesirable electrode/electrolyte reactions caused by the greater surface area, low volumetric energy densities due to the inferior packing of nanoparticles, and the high cost of complicated synthesis processes.[2,4] There has already been a variety of approaches made to overcome some of these issues such as forming composites with carbon or a conductive agent, or using assembled, hollow, or core−shell structures.[9−13] More recently, self-assembled structures with a carbon coating have emerged as a promising candidate for the cathode and anode material of lithium-ion batteries (LIBs). Such self-assembled structures have the potential to not only reduce the transport pathways of Li^+ ions and electrons but also reduce the unwanted side reactions between electrodes and the electrolyte.[14−17] Moreover, their porous nature provides a volume of free space that can help accommodate the intense volume expansion of electrodes during cycling.[15−17] The carbon coating acts to improve the overall electrical conductivity and mechanical strength, ensures the formation of a stable solid electrolyte interface (SEI), and helps prevent self-aggregation of the nanoparticles.[9,18,19] Although various methods have been previously developed for fabricating a self-assembled structure, these approaches tend to either be based on inert conditions or rely on a complex high temperature, high pressure process.[17,20−26] In this study, a simple one-step method for the graphene oxide assisted synthesis of a hierarchical self-assembled zinc oxide (SAZO) is described, and the suitability of the resulting material as LIB anode is evaluated. Zinc oxide (ZnO) has previously been studied as a negative electrode in LIBs because of its low cost, good chemical stability, and high theoretical capacity (988 mAh g^{-1}).[27,28] Other groups have reported ZnO incorporated graphene oxide (GO) composites as anode materials in LIB, using the blend of GO and ZnO.[29,30] Here, we demonstrated the simple synthetic method for multiscale nano-micro ZnO structures with hierarchical morphology including the self-assembled ZnO (SAZO) nanoaggregates by using GOs as templates. In addition, these hierarchical structures showed excellent performance as LIB anode materials compared to other ZnO anode materials that had been previous reported.[29,31,32]

2. EXPERIMENTAL SECTION

Synthesis of SAZO@GO. Graphene oxide (GO) was prepared from graphite powder (Bay Carbon Inc.) by a modified Hummers method. In a typical synthesis, zinc acetate ($(CH_3CO_2)_2Zn$, 0.92 g) was added to

Received: September 17, 2015
Revised: October 26, 2016
Published: November 2, 2016

ACS Publications © 2016 American Chemical Society

DOI: 10.1021/acs.chemmater.5b03587
Chem. Mater. 2016, 28, 8498−8503

N,*N*-dimethylformamide (DMF, 200 mL). The mixture was stirred for 20 min at the room temperature. Graphene oxide (GO, 40 mg) was also dissolved in 50 mL of DMF and sonicated for 30 min. Then, the graphene oxide solution was added to the zinc acetate solution under vigorous stirring. The colorless solution changed to a dark blue color. The mixture was heated to 95−125 °C under continuous stirring. After keeping for 5 h at 70−125 °C, the result products were isolated by the addition of ethanol and deionized (DI) water, followed by centrifugation. The resulting powder was transferred to a quartz tube furnace and annealed at 500 °C with argon gas for 3 h.

Synthesis of DLZO@GO. Typical synthesis of DLZO@GO is almost the same with that of SAZO@GO. Reactions were also carried out in which the solution ratio of GO solution was systematically varied in the range 0.25−4 of DMF:DI water ratio. The entire process was carried out as described for the SAZO@GO.

Synthesis of DLZO, ZONC without GO. In a typical synthesis, zinc acetate ($(CH_3CO_2)_2Zn$, 0.92 g) was added to 250 ml of DMF or mixed solution (DMF:DI water = 1:4). The mixture was heated to 125 °C under continuous stirring. After keeping for 5 h at 125 °C, the resulting products were isolated by the addition of ethanol and DI water, followed by centrifugation. The powders were dried in a vacuum oven at 70 °C for 10 h.

Synthesis Process of ZnO in Inert Condition. The synthesis was performed in an argon atmosphere using standard Schlenk line techniques. DMF (250 mL) was added to a three-neck flask containing zinc acetate ($(CH_3CO_2)_2Zn$, 0.92 g). Then, the solution was heated to 125 °C and kept for 5 h at the same temperature with continuous stirring.

Characterization. The morphologies of zinc oxides were examined using a field-emission transmission electron microscope (TEM; JEOL JEM-2100) at an acceleration voltage of 200 kV and a scanning electron microscope (Cold FE-SEM; Hitachi s-4800) at a voltage of 10.0 kV. The X-ray diffraction (XRD) patterns were collected on a D/MAZX 2500V/PC (Rigaku) using Cu−Kα radiation (λ = 1.5405 Å) operated for 2θ = 10−80° and scan rate = 2° min^{-1}. Thermogravimetric analysis (TGA) of samples with GO was measured by an SDT Q600 (TA Instruments). The Raman spectra were collected by alpha300R (WITec).

Electrochemical Investigation. Electrochemical measurements were performed on a 2032 coin-type half-cell, where Li metal foil was used as the counter electrode. Working electrodes were fabricated by mixing the active materials (80 wt %), Super P (10 wt %) and polyvinylidene fluoride (PVDF, 10 wt %) binder in 1-methyl-2-pyrrolidone. 2032 coin-type half-cells were assembled in an Ar-filled glovebox. The electrolyte was 1.3 M LiPF6 in a 3:7 volume mixture of ethylene carbonate (EC) and diethyl carbonate (DEC), and a separator was used a microporous polyethylene film. Galvanostatic charge and discharge cycling was performed in the potential window from 0.02 to 3.0 V (vs Li/Li^+) by using a WonATech WBCS 3000 battery measurement system. The cyclic voltammetry experiment was also measured in the potential window from 0.02 to 3.0 V (vs Li/Li^+) by using a WonATech WBCS 3000 battery measurement system.

The electrochemical impedance spectroscopy (EIS) data were collected using a signal with an amplitude of 10 mV and a frequency range from 100 kHz to 5 mHz. The half-cells were discharged to 0.5 V (vs Li/Li^+) at 500 mA g^{-1}, and a constant voltage of 0.5 V was applied until the current decreased to 10 mA g^{-1}. Then, the cells were allowed to rest for 3 h.

3. RESULT AND DISCUSSION

The method used to synthesize the SAZO and GO nanocomposite is illustrated in Scheme 1. The SAZO@GO composite is obtained by simply heating a mixture of zinc acetate and graphene oxide in DMF above 95 °C under atmospheric pressure, GO having been prepared from natural graphite powder by a modified Hummers method.[33]

Spontaneous hydrolysis and condensation of zinc acetate precursors in DMF occurs due to the moisture in the air and trace of water in the solvent, resulting in the formation of ZnO

Scheme 1. Illustration Depicting the Preparation of SAZO and GO Nanocomposite

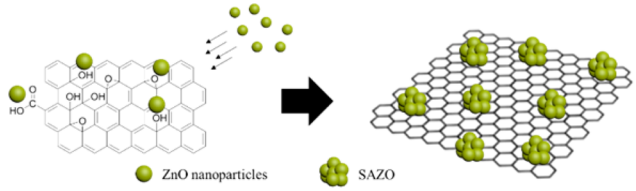

nanoparticles. Consequently, the dangling bond in the surface of ZnO nanoparticles could be stabilized by interacting with functional groups (COOH, OH) of GO.[34] Then, colloidal ZnO nanoparticles in DMF were going to assemble into chemically linked ZnO with the GO, resulting in the secondary hierarchical structures. In the absence of GO, the ZnO does not form a self-assembled hierarchical morphology, but rather agglomerates of nanoparticles (Figure S1).

The results of TEM and SEM shown in Figure 1 and Figure S2 confirm that the ZnO particles on the surface of GO have a

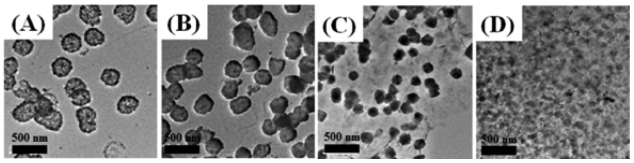

Figure 1. TEM images of ZnO@GO synthesized at temperatures of (A) 125 °C, (B) 95 °C, (C) 85 °C, and (D) 45 °C.

hierarchical morphology with diameters ranging from 240 to 280 nm depending on the temperature of synthesis. Therefore, controllable synthesis of a self-assembled nanocomposite is possible through assistance of GO.

Figure S3 depicts the XRD patterns of ZnO@GO composites with varying synthesis temperatures. This demonstrates that a hexagonal phase pure ZnO is formed when the synthesis temperature is above 95 °C; however, impurities are detected with synthesis temperatures below 85 °C. The TEM images suggest that impurities may still be present in SAZO@GO composites generated at more than 85 °C; however, there is a notable change in particle size between the 130 to 190 nm of the 85 °C sample and the 240 to 280 nm of those samples produced at 95 °C or above. In order to further understand the mechanism of ZnO formation, an aliquot of the reaction solution was taken at different stages of the process (Figure S4). TEM images of those aliquots removed while the temperature was still below 70 °C indicate that ZnO clusters are generated on the GO, but some impurities still exist. Pure self-assembled materials are identified, ranging in size from 110 to 150 nm, once the temperature reaches 95 °C. These particles go on to form the larger SAZO particles, reaching their maximum size of 280 nm after aging for an hour.

Moisture is also a very significant factor deciding the final morphology of the ZnO, as it influences both hydrolysis and condensation. Synthesis was, therefore, conducted under inert conditions without moisture, though this simply inhibited hydrolysis and condensation reaction to the extent that ZnO was not formed (Figure S5). In contrast, the introduction of additional DI water caused a more intense and exothermic hydrolysis and condensation reaction. If the moisture in the air and DMF at room temperature is assumed to be a negligible quantity, then 10 mL of DI water is sufficient to form a self-assembled hierarchical ZnO. However, a quantity of DI water

DOI: 10.1021/acs.chemmater.5b03587
Chem. Mater. 2016, 28, 8498−8503

greater than 25 mL results in an irregular ZnO morphology with diameters from 100 to 300 nm. Furthermore, increasing the DI water to 50 mL resulted in a doughnut-like morphology as the ZnO was increasingly etched from the inside with reaction time (Figures S6 and S7). The high amount of water in the solvent system accelerates the rate of hydrolysis and condensation process, and as a result, a large sub-micrometer sized ZnO structure not self-assembled nanoparticles was synthesized.

XRD analysis of all samples, however, indicated that only a hexagonal phase ZnO was present (Figure S8).

TGA of SAZO@GO (Figure 2A) conducted at temperatures up to 700 °C in air reveals that the weight fraction of ZnO in the

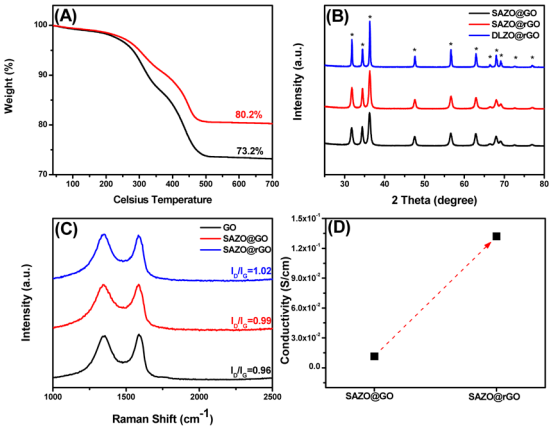

Figure 2. (A) TGA curves showing the temperature dependence of SAZO@GO synthesis: red line 125 °C, black line 95 °C. (B) XRD patterns of self-assembled ZnO and doughnut-like ZnO samples. (C) Raman spectra of GO and self-assembled ZnO with GO. (D) Electrical conductivity of SAZO@GO and SAZO@rGO.

composite is dependent on the synthesis temperature. The small mass loss below 130 °C can be explained by the thermal removal of absorbed water, while the large mass loss of GO above 200 °C is the result of thermal decomposition. The TGA analysis confirms that the GO is entirely eliminated below 500 °C (Figure S9). Furthermore, SEM images confirm that the GO is eliminated without damage to the hierarchical morphology (Figure S10). Consequently, a high reaction temperature of 125 °C results in a ZnO weight fraction of 80.2% in the composite, which is higher than that obtained using a lower temperature (95 °C).

Though the GO is primarily considered as a host for self-assembly, when reduced, it also proves to be an effective additive for increasing electrical conductivity. Hybrid nanostructures incorporating reduced graphene oxide (rGO) sheets have been previously reported to hamper the agglomeration of nanoparticles on during cycling and improve the overall electrical conductivity.[10,35−37] As a result, such hybrid nanostructures typically exhibit a high specific capacity and long cycle stability.[35−38] The reduction of GO was achieved by transferring the samples to a quartz tube furnace and annealing them for 3 h at 500 °C under an argon atmosphere. The XRD patterns of the resulting SAZO@rGO as shown in Figure 2B demonstrate that a hexagonal ZnO structure was retained after calcination, consistent with the reference standard card (JCPDS No. 36-1451).

To prove the reduction of GO, Raman spectra of GO and SAZO@GO before and after calcination were obtained, as shown in Figure 2C. In all samples, the two major peaks of the D and G bands can be observed. The D and G bands of GO are located at around 1588 and 1355 cm^{-1}; however, the G band is red-shifted to 1585 cm^{-1} in SAZO@GO and to 1583 cm^{-1} in SAZO@rGO. This suggests that the synthesis process itself contributes to a shift in the G band and that additional heat treatment merely creates a further shift in the G band. The gradual increase in the I_D/I_G band intensity ratio from GO to SAZO@rGO suggests a high degree of GO reduction by heat treatment.[39,40]

Analysis of electrical conductivity using the van der Pauw method was also used to confirm the reduction of GO, the resulting data shown in Figure 2D.[41] The SAZO@GO powders have an electrical conductivity of 1.15×10^{-2} S cm^{-1}, which is dramatically increased to 1.32×10^{-1} S cm^{-1} after heat treatment. This provides fairly conclusive evidence that GO is reduced to rGO and means that rGO can be used to improve the poor electrical conductivity of ZnO.

Electrochemical measurements were performed using a 2032 coin-type half-cell, in which Li metal foil was used as the counter electrode. The lithiation process of ZnO involves two separate reactions, a conversion reaction and an alloying reaction.[27,28]

In the conversion reaction, ZnO is converted to zinc metal and amorphous Li_2O is generated. In the subsequent alloying reaction, the generated zinc metal can become Li_2Zn_5, $LiZn_2$, Li_2Zn_3, and LiZn by reacting with lithium ions.[27,28,31]

The beneficial role of rGO in electrical networking is confirmed by EIS measurements for the electrodes of ZnO nanoparticle clusters without rGO (ZONC) and with rGO (SAZO@rGO). The Nyquist plot for ZONC (Figure S11) consists of two semicircles at high and mid frequency and the sloping Warburg tail at low frequency. The size of the high-frequency semicircle corresponds with the resistance associated with electronic conductivity of composite electrodes and/or migration of Li ions through the SEI layers on ZnO.[42,43] The mid-frequency semicircle reflects the charge-transfer resistance at ZnO−electrolyte interfaces.[42] As compared to the result for ZONC, the spectra for SAZO/rGO exhibits a much smaller high-frequency semicircle and disappearance of the mid-frequency semicircle, which is interpreted by enhanced electronic conductivity and charge-transfer kinetics by the rGO-networking, respectively.

Figure 3A shows that the electrochemical behavior of the SAZO@rGO electrodes, as characterized by cyclic voltammo-

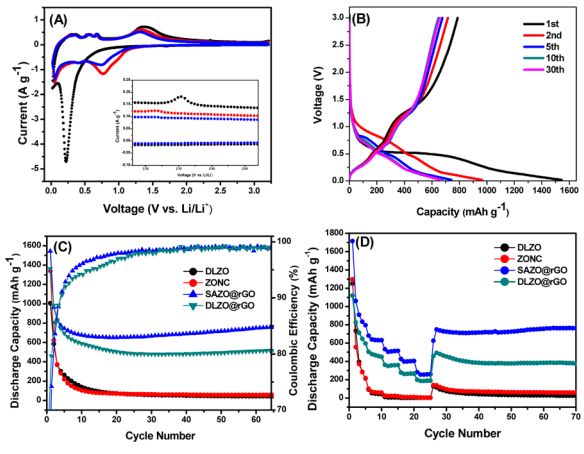

Figure 3. (A) Cyclic voltammograms of a SAZO@rGO electrode at a scanning rate of 0.2 mV s^{-1}. (B) Discharge−charge curves for SAZO@rGO. (C) Cycling performance of ZnO electrodes at a current density of 100 mA g^{-1}. (D) Rate performance of ZnO electrodes.

DOI: 10.1021/acs.chemmater.5b03587
Chem. Mater. 2016, 28, 8498−8503

grams (CV) at a scanning rate of 0.2 mV s^{-1}. In the first cathodic process, only a singular strong peak can be identified in the range of 0.5−0.1 V; this range is related to the reduction of ZnO to Zn at >0.3 V, the lithium−zinc alloy reaction at <0.3 V, and the formation of a gel-like SEI layer.[28] Although the potentials of these reactions are, strictly speaking, quite different, they are nonetheless very close and, therefore, present as just one strong peak. In the first anodic process, a number of peaks are observed at various voltages. Those peaks located at 0.35, 0.55, 0.68, and 1.36 V are likely related to the dealloying reactions of Li−Zn alloys, while the weak peak at 2.35 V is indicative of the conversion reaction of Zn to ZnO.[27,28] In subsequent cycles, the conversion reaction peak varies due to activation processes.

Figure 3B,C show the cycling performance of ZnOs with rGO in the 0.02−3.00 V range (vs Li^+/Li) at a current density of 100 mA g^{-1}. For comparison, galvanostatic discharge/charge experimental data for the zinc oxide nanoparticle cluster (ZONC) and doughnut-like zinc oxide (DLZO) electrode without rGO under similar conditions are also presented. The first discharge capacity of all samples exceeds the theoretical value of 988 mAh g^{-1}, which is believed to be due to decomposition of the electrolyte upon reduction at low potential in the conversion reaction.[44,45] The specific capacity of all electrodes, with rGO or without rGO, rapidly decreases during the initial cycling but rapidly rebounds after a certain number of cycles due to an as yet unidentified activation process.[15]

After 65 cycles, the reversible discharge capacities of the SAZO@rGO and DLZO@rGO electrodes were 752.8 and 517.7 mAh g^{-1}, respectively, whereas the ZONC and DLZO electrodes without rGO showed disastrous performance. In the case of SAZO@rGO and DLZO@rGO electrodes, the rGO served to improve the electrical conductivity and leads to better retention; however, the insulating nature of ZONC and DLZO inhibits cycling retention and causes the capacity to fade after the initial 10 cycles. The initial Coulombic efficiencies (CEs) of both SAZO@rGO and DLZO@rGO electrodes were very poor (51.0% and 65.7%) due to decomposition of the electrolyte in the first cycle, the formation of an SEI layer, and an undetermined irreversible reaction; however, the CEs of both electrodes rapidly increased during the initial 10 cycles and eventually reached up to 99.1%. The more rapid increase in CEs seen with the SAZO@rGO electrode means that it achieved faster stabilization and electrode activation than the DLZO@rGO electrode. More importantly, the cycling performance of ZnOs with rGO in the 0.02−3.00 V range (vs Li^+/Li) at a current density of 500 mA g^{-1} shows a direct difference in the cyclic stability of both electrodes (Figure S12). In the case of the SAZO@rGO electrode, for example, the discharge capacity is stabilized over a long number of cycles despite an initial decrease in capacity. Conversely, the cyclic capacity of the DLZO@rGO electrode decreased rapidly after 30 cycles and exhibited a particularly poor cyclic stability at a high current density (500 mA g^{-1}).

This phenomenon was also observed in the cycling performance of SAZO@rGO and DLZO@rGO electrodes at various current densities. After a rapid fading of capacity during the initial cycle at low current (100 mA g^{-1}) due to activation of the electrodes, the capacity remained stable during cycling at various current densities with all samples, though the SAZO@rGO electrode exhibited better reversible performance under all the conditions. The discharge capacities of the SAZO@rGO electrode were 631.2, 515.9, 404.4, and 259.7 mAh g^{-1} at current densities of 250, 500, 1000, and 2000 mA g^{-1}, respectively, whereas, for the DLZO@rGO electrode, these values were 449.8, 360.4, 267.8, and 190.0 mAh g^{-1}. When the current density reverted to 100 mA g^{-1} during cycling, 2000 mA g^{-1}, the reversible capacities of the SAZO@rGO and DLZO@rGO electrodes were >700 mAh g^{-1} and 400 mAh g^{-1}, respectively.

The reason for the higher and more stable performance of the SAZO@rGO electrode is attributable to benefits of a hierarchical self-assembled structure. Specifically, such as the structure incorporates a void space that can act as a buffer to the intense volume expansion that occurs during cycling.[15] Furthermore, the SAZO@rGO electrode can form a stable SEI layer on its outer surface.[15] Figure 4 shows SEM images of SAZO@rGO and

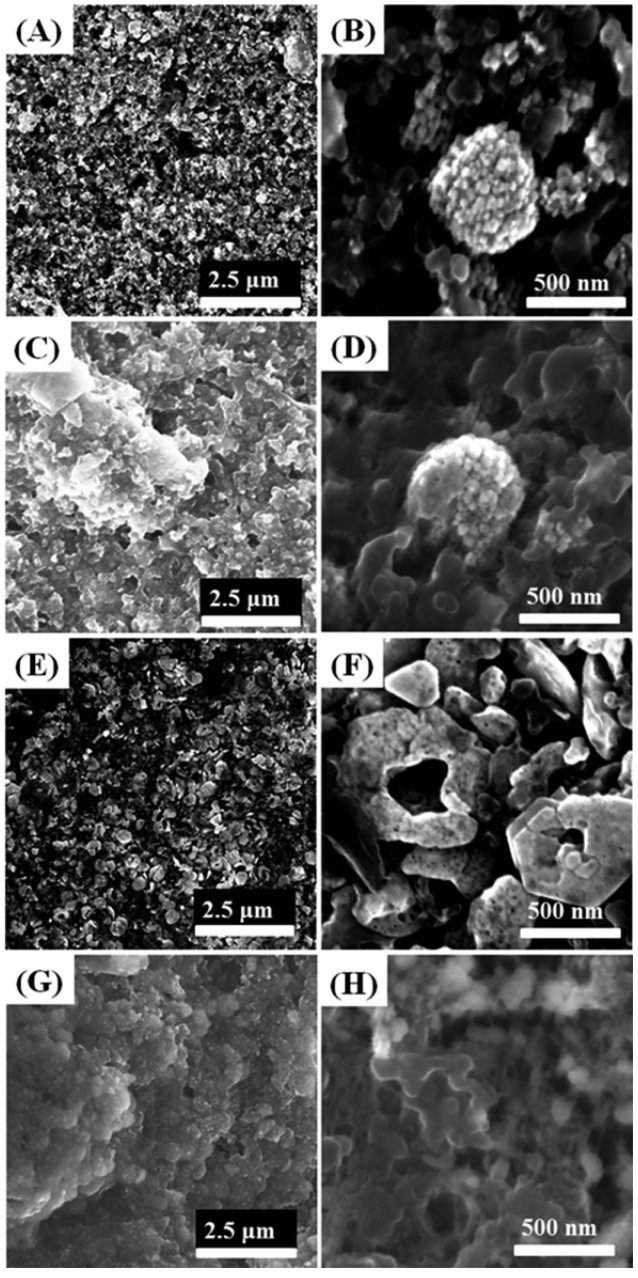

Figure 4. SEM images of (A, B) a bare SAZO@rGO electrode and (E, F) a bare DLZO@rGO electrode. SEM images of (C, D) a SAZO@rGO electrode and (G, H) a bare DLZO@rGO electrode after 100 cycles at a current density of 500 mA g^{-1}.

DOI: 10.1021/acs.chemmater.5b03587
Chem. Mater. 2016, 28, 8498−8503

DLZO@rGO electrodes before and after cycling, in which the SAZO@rGO electrode clearly maintains its morphology after 100 cycles, whereas the DLZO@rGO electrode cannot maintain its doughnut-like structure.

4. CONCLUSION

In summary, a simple method for the hierarchical self-assembly of ZnO was successfully developed by using GO. Though the GO plays a leading role in creating the self-assembled structure, it also serves to overcome the electrically insulating nature of ZnO. As anodes in a lithium-ion battery, the hierarchical structure exhibits excellent cycle stability, higher cycling performance, and better rate capabilities than a doughnut-like ZnO structure. Furthermore, self-assembled ZnO with rGO offers advantages in terms of high electrical conductivity, short diffusion length, a stable SEI layer, and sufficient buffer space to accumulate the intense volume expansion during cycling.

■ ASSOCIATED CONTENT

Supporting Information

The Supporting Information is available free of charge on the ACS Publications website at DOI: 10.1021/acs.chemmater.5b03587.

TEM images of ZnO nanoparticle clusters and doughnut-like ZnO; SEM images and XRD patterns of ZnO@rGO with various synthesis temperatures; a time series of TEM images of ZnO@rGO; TEM images of the resultant product after ZnO synthesis under inert conditions; SEM images, TEM images, and XRD patterns of ZnO@GO at 85 °C with varying cosolvent ratios; TGA data and SEM images of SAZO@GO before and after calcination at 500 °C in air; EIS data for SAZO@rGO compared with ZO; and galvanostatic discharge−charge voltage profiles of SAZO@rGO and DLZO@rGO (PDF)

■ AUTHOR INFORMATION

Corresponding Author

*E-mail: jnpark@unist.ac.kr.

Notes

The authors declare no competing financial interest.

■ ACKNOWLEDGMENTS

This work was supported by the New & Renewable Energy Core Technology Program of the Korea Institute of Energy Technology Evaluation and Planning (KETEP), granted financial resource from the Ministry of Trade, Industry & Energy, Republic of Korea (No. 20133030000180).

■ REFERENCES

(1) Wang, Y.; Chen, M.; Zhou, F.; Ma, E. High Tensile Ductility in a Nanostructured Metal. *Nature* **2002**, *419*, 912−915.

(2) Aricò, A. S.; Bruce, P.; Scrosati, B.; Tarascon, J.-M.; van Schalkwijk, W. Nanostructured Materials for Advanced Energy Conversion and Storage Devices. *Nat. Mater.* **2005**, *4*, 366−377.

(3) Ovid'ko, I. A. Materials Science. Deformation of Nanostructures. *Science* **2002**, *295*, 2386−2386.

(4) Bruce, P. G.; Scrosati, B.; Tarascon, J.-M. Nanomaterials for Rechargeable Lithium Batteries. *Angew. Chem., Int. Ed.* **2008**, *47*, 2930−2946.

(5) Li, N.; Martin, C. R.; Scrosati, B. Nanomaterial-Based Li-Ion Battery Electrodes. *J. Power Sources* **2001**, *97*−*98*, 240−243.

(6) Odani, A.; Nimberger, A.; Markovsky, B.; Sominski, E.; Levi, E.; Kumar, V. G.; Motiei, M.; Gedanken, A.; Dan, P.; Aurbach, D. Development and Testing of Nanomaterials for Rechargeable Lithium Batteries. *J. Power Sources* **2003**, *119*−*121*, 517−521.

(7) Liu, H. K.; Wang, G. X.; Guo, Z.; Wang, J.; Konstantinov, K. Nanomaterials for Lithium-Ion Rechargeable Batteries. *J. Nanosci. Nanotechnol.* **2006**, *6*, 1−15.

(8) Lee, K. T.; Cho, J. Roles of Nanosize in Lithium Reactive Nanomaterials for Lithium Ion Batteries. *Nano Today* **2011**, *6*, 28−41.

(9) Lee, S.; Cho, Y.; Song, H.-K.; Lee, K. T.; Cho, J. Carbon-Coated Single-Crystal $LiMn_2O_4$ Nanoparticle Clusters as Cathode Material for High-Energy and High-Power Lithium-Ion Batteries. *Angew. Chem., Int. Ed.* **2012**, *51*, 8748−8752.

(10) Wang, H.; Cui, L.-F.; Yang, Y.; Casalongue, H. S.; Robinson, J. T.; Liang, Y.; Cui, Y.; Dai, H. Mn_3O_4−Graphene Hybrid as a High-Capacity Anode Material for Lithium Ion Batteries. *J. Am. Chem. Soc.* **2010**, *132*, 13978−13980.

(11) Wang, J.; Sun, X. Understanding and Recent Development of Carbon Coating on $LiFePO_4$ cathode Materials for Lithium-Ion Batteries. *Energy Environ. Sci.* **2012**, *5*, 5163−5185.

(12) Liu, J.; Xue, D. Hollow Nanostructured Anode Materials for Li-Ion Batteries. *Nanoscale Res. Lett.* **2010**, *5*, 1525−1534.

(13) Wang, Y.; Wang, Y.; Hosono, E.; Wang, K.; Zhou, H. The Design of a $LiFePO_4$/Carbon Nanocomposite with a Core−Shell Structure and Its Synthesis by an in Situ Polymerization Restriction Method. *Angew. Chem., Int. Ed.* **2008**, *47*, 7461−7465.

(14) Lu, Y.; Tu, J. P.; Xiang, J. Y.; Wang, X. L.; Zhang, J.; Mai, Y. J.; Mao, S. X. Improved Electrochemical Performance of Self-Assembled Hierarchical Nanostructured Nickel Phosphide as a Negative Electrode for Lithium Ion Batteries. *J. Phys. Chem. C* **2011**, *115*, 23760−23767.

(15) Lee, S. H.; Yu, S.-H.; Lee, J. E.; Jin, A.; Lee, D. J.; Lee, N.; Jo, H.; Shin, K.; Ahn, T.-Y.; Kim, Y. W.; et al. Self-Assembled Fe_3O_4 Nanoparticle Clusters as High-Performance Anodes for Lithium Ion Batteries via Geometric Confinement. *Nano Lett.* **2013**, *13*, 4249−4256.

(16) Lee, J. E.; Yu, S.-H.; Lee, D. J.; Lee, D.-C.; Han, S. I.; Sung, Y.-E.; Hyeon, T. Facile and Economical Synthesis of Hierarchical Carbon-Coated Magnetite Nanocomposite Particles and Their Applications in Lithium Ion Battery Anodes. *Energy Environ. Sci.* **2012**, *5*, 9528−9533.

(17) Magasinski, A.; Dixon, P.; Hertzberg, B.; Kvit, A.; Ayala, J.; Yushin, G. High-Performance Lithium-Ion Anodes Using a Hierarchical Bottom-Up Approach. *Nat. Mater.* **2010**, *9*, 353−358.

(18) Jang, B.; Park, M.; Chae, O. B.; Park, S.; Kim, Y.; Oh, S. M.; Piao, Y.; Hyeon, T. Direct Synthesis of Self-Assembled Ferrite/Carbon Hybrid Nanosheets for High Performance Lithium-Ion Battery Anodes. *J. Am. Chem. Soc.* **2012**, *134*, 15010−15015.

(19) Oh, S. W.; Myung, S. T.; Oh, S. M.; Oh, K. H.; Amine, K.; Scrosati, B.; Sun, Y. K. Double Carbon Coating of $LiFePO_4$ as High Rate Electrode for Rechargeable Lithium Batteries. *Adv. Mater.* **2010**, *22*, 4842−4845.

(20) Xu, X.; Cao, R.; Jeong, S.; Cho, J. Spindle-Like Mesoporous A-Fe_2O_3 Anode Material Prepared From MOF Template for High-Rate Lithium Batteries. *Nano Lett.* **2012**, *12*, 4988−4991.

(21) Sun, Y.; Hu, X.; Luo, W.; Huang, Y. Self-Assembled Hierarchical MoO_2/Graphene Nanoarchitectures and Their Application as a High-Performance Anode Material for Lithium-Ion Batteries. *ACS Nano* **2011**, *5*, 7100−7107.

(22) Jin, S.; Deng, H.; Long, D.; Liu, X.; Zhan, L.; Liang, X.; Qiao, W.; Ling, L. Facile Synthesis of Hierarchically Structured Fe_3O_4/Carbon Micro-Flowers and Their Application to Lithium-Ion Battery Anodes. *J. Power Sources* **2011**, *196*, 3887−3893.

(23) Yang, H.; Wu, X.-L.; Cao, M.-H.; Guo, Y.-G. Solvothermal Synthesis of $LiFePO_4$ Hierarchically Dumbbell-Like Microstructures by Nanoplate Self-Assembly and Their Application as a Cathode Material in Lithium-Ion Batteries. *J. Phys. Chem. C* **2009**, *113*, 3345−3351.

(24) Demir-Cakan, R.; Hu, Y.-S.; Antonietti, M.; Maier, J.; Titirici, M.-M. Facile One-Pot Synthesis of Mesoporous SnO_2 Microspheres via Nanoparticles Assembly and Lithium Storage Properties. *Chem. Mater.* **2008**, *20*, 1227−1229.

(25) Lin, Y.-S.; Tsai, M.-C.; Duh, J.-G. Self-Assembled Synthesis of Nanoflower-Like $Li_4Ti_5O_{12}$ for Ultrahigh Rate Lithium-Ion Batteries. *J. Power Sources* **2012**, *214*, 314−318.

DOI: 10.1021/acs.chemmater.5b03587
Chem. Mater. 2016, 28, 8498−8503

(26) Lu, Z.; Yin, Y. Colloidal Nanoparticle Clusters: Functional Materials by Design. *Chem. Soc. Rev.* **2012**, *41*, 6874−6887.
(27) Huang, X. H.; Xia, X. H.; Yuan, Y. F.; Zhou, F. Porous ZnO Nanosheets Grown on Copper Substrates as Anodes for Lithium Ion Batteries. *Electrochim. Acta* **2011**, *56*, 4960−4965.
(28) Chae, O. B.; Park, S.; Ryu, J. H.; Oh, S. M. Performance Improvement of Nano-Sized Zinc Oxide Electrode by Embedding in Carbon Matrix for Lithium-Ion Batteries. *J. Electrochem. Soc.* **2013**, *160*, A11−A14.
(29) Chen, Y.-L.; Hu, Z.-A.; Chang, Y.-Q.; Wang, H.-W.; Zhang, Z.-Y.; Yang, Y.-Y.; Wu, H.-Y. Zinc Oxide/Reduced Graphene Oxide Composites and Electrochemical Capacitance Enhanced by Homogeneous Incorporation of Reduced Graphene Oxide Sheets in Zinc Oxide Matrix. *J. Phys. Chem. C* **2011**, *115*, 2563−2571.
(30) Hsieh, C.-T.; Lin, C.-Y.; Chen, Y.-F.; Lin, J.-S. Synthesis of ZnO@ Graphene composites as anode materials for lithium ion batteries. *Electrochim. Acta* **2013**, *111*, 359−365.
(31) Zhang, C. Q.; Tu, J. P.; Yuan, Y. F.; Huang, X. H.; Chen, X. T.; Mao, F. Electrochemical Performances of Ni-Coated ZnO as an Anode Material for Lithium-Ion Batteries. *J. Electrochem. Soc.* **2007**, *154*, A65−A69.
(32) Lu, T.; Pan, L.; Li, H.; Zhu, G.; Lv, T.; Liu, X.; Sun, Z.; Chen, T.; Chua, D. H. C. Microwave-assisted synthesis of graphene−ZnO nanocomposite for electrochemical supercapacitors. *J. Alloys Compd.* **2011**, *509*, 5488−5492.
(33) Marcano, D. C.; Kosynkin, D. V.; Berlin, J. M.; Sinitskii, A.; Sun, Z.; Slesarev, A.; Alemany, L. B.; Lu, W.; Tour, J. M. Improved Synthesis of Graphene Oxide. *ACS Nano* **2010**, *4*, 4806−4814.
(34) Son, D. I.; Kwon, B. W.; Park, D. H.; Seo, W.-S.; Yi, Y.; Angadi, B.; Lee, C.-L.; Choi, W. K. Emissive ZnO−Graphene Quantum Dots for White-Light-Emitting Diodes. *Nat. Nanotechnol.* **2012**, *7*, 465−471.
(35) Yu, S.-H.; Conte, D. E.; Baek, S.; Lee, D.-C.; Park, S. K.; Lee, K. J.; Piao, Y.; Sung, Y.-E.; Pinna, N. Structure-Properties Relationship in Iron Oxide-Reduced Graphene Oxide Nanostructures for Li-Ion Batteries. *Adv. Funct. Mater.* **2013**, *23*, 4293−4305.
(36) Wang, H.; Yang, Y.; Liang, Y.; Cui, L.-F.; Sanchez Casalongue, H.; Li, Y.; Hong, G.; Cui, Y.; Dai, H. $LiMn_{1-x}Fe_xPO_4$ Nanorods Grown on Graphene Sheets for Ultrahigh-Rate-Performance Lithium Ion Batteries. *Angew. Chem., Int. Ed.* **2011**, *50*, 7364−7368.
(37) Zhu, X.; Zhu, Y.; Murali, S.; Stoller, M. D.; Ruoff, R. S. Nanostructured Reduced Graphene Oxide/Fe_2O_3Composite as a High-Performance Anode Material for Lithium Ion Batteries. *ACS Nano* **2011**, *5*, 3333−3338.
(38) Yang, S.; Feng, X.; Ivanovici, S.; Müllen, K. Fabrication of Graphene-Encapsulated Oxide Nanoparticles: Towards High-Performance Anode Materials for Lithium Storage. *Angew. Chem., Int. Ed.* **2010**, *49*, 8408−8411.
(39) Li, J.; Xiao, G.; Chen, C.; Li, R.; Yan, D. Superior Dispersions of Reduced Graphene Oxide Synthesized by Using Gallic Acid as a Reductant and Stabilizer. *J. Mater. Chem. A* **2013**, *1*, 1481−1487.
(40) Cuong, T. V.; Pham, V. H.; Tran, Q. T.; Hahn, S. H.; Chung, J. S.; Shin, E. W.; Kim, E. J. Photoluminescence and Raman Studies of Graphene Thin Films Prepared by Reduction of Graphene Oxide. *Mater. Lett.* **2010**, *64*, 399−401.
(41) Jung, Y. S.; Cavanagh, A. S.; Dillon, A. C.; Groner, M. D.; George, S. M.; Lee, S.-H. Enhanced Stability of $LiCoO_2$ Cathodes in Lithium-Ion Batteries Using Surface Modification by Atomic Layer Deposition. *J. Electrochem. Soc.* **2010**, *157*, A75−A81.
(42) Bard, A. J.; Faulkner, L. R. *Electrochemical Methods: Fundamentals and Applications*, 2nd ed.; John Wiley & Sons, Inc.: New York, 2001.
(43) Gaberscek, M.; Moskon, J.; Erjavec, B.; Dominko, R.; Jamnik, J. *Electrochem. Solid-State Lett.* **2008**, *11*, A170−A174.
(44) Cabana, J.; Monconduit, L.; Larcher, D.; Palacín, M. R. Beyond Intercalation-Based Li-Ion Batteries: the State of the Art and Challenges of Electrode Materials Reacting Through Conversion Reactions. *Adv. Mater.* **2010**, *22*, E170−E192.
(45) Ponrouch, A.; Taberna, P.-L.; Simon, P.; Palacín, M. R. On the Origin of the Extra Capacity at Low Potential in Materials for Li Batteries Reacting Through Conversion Reaction. *Electrochim. Acta* **2012**, *61*, 13−18.

DOI: 10.1021/acs.chemmater.5b03587
Chem. Mater. 2016, 28, 8498−8503